


Diffusive homeostasis in a self-organizing recurrent neural network: Spatially dependent interaction as a determinant of neural activity and plasticity

Fabian Schubert¹, Daniel Miner¹[‡], Jochen Triesch¹[†],

1 Frankfurt Institute for Advanced Studies, Frankfurt am Main, Germany

 This author performed parts of the programming, analysis and writing and contributed to the conceptualization.

[‡]This author performed parts of the programming, provided significant expertise and consultation and contributed to the conceptualization.

[†]This author provided significant expertise and consultation and contributed to the conceptualization.

* E-mail: fschubert@fias.uni-frankfurt.de

Abstract

The topology of cortical networks is subject to constant change and the mechanisms involved in these dynamics are strongly influenced by the timing and intensity of neural spiking within these networks. Consequently, the success of a realistic biologically based computational model of synaptic structure and self-organization largely depends on an accurate modeling of neural activity. Experiments have found evidence for a broad, log-normal distribution of firing rates among cortical neurons. It is suggested that this heterogeneity of cortical activity has a functional role in the context of stimulus encoding and the formation of stable subpopulations of synapses.

Building upon on a self-organizing spiking neural network (LIF-SORN), we replaced an intrinsic homeostatic control system used in earlier versions by a mechanism based on the diffusion of a neurotransmitter across the nervous tissue. The model of diffusive homeostasis was adopted from a previously published theoretical study. The main goal of this modification was to allow for the aforementioned broad and heavy tailed distribution of firing rates among the excitatory neural population, which could not be achieved by the formerly used single-cell homeostatic mechanism, binding firing rates of all neurons to a fixed target value. The resulting statistical features of spiking activity were positive regarding the desired firing rate statistics. Furthermore, we compared both homeostatic mechanisms with respect to features of synaptic network structures emerging throughout the simulation. Apart from the preservation of earlier reported non-random topological features, we found that diffusive homeostasis allowed for the emergence of neurons with strong outgoing synaptic efficacies. We could relate this feature of synaptic topology to the imposed spatial structure of the neural population by means of an analytic approach to the diffusive homeostatic steady state.

Author summary

We improved a model of self-organizing cortical network by implementing a model known as *diffusive homeostasis*, which is capable of controlling neuronal activity based on the diffusion of a neurotransmitter. Previously reported non-random features of the

network structure were preserved while allowing for a broader distribution of neuronal firing rates. Our modifications also led to the accumulation of strong synapses to a small subgroup of highly active neurons. By further analyzing the diffusive control, we found that the statistics of firing rates within the network are strongly affected by the structure of the neurons' positions. This raised the question whether the spatial structure of a cortical network, in particular fluctuations of neuronal densities, can influence activity not only by means of distance-dependent synaptic connection probabilities, but also through diffusive interaction.

Introduction

Many theoretical studies in recent years have addressed the question how cortical network activity and synaptic structure forms and organizes itself, based on a limited set of experimentally observed basic mechanisms and compartments [1–4]. Typical elements of these models include some type of hebbian-type rule of synaptic plasticity, especially spike-timing-dependent plasticity in the case of spiking networks [5], and some type of control that limits synaptic efficacies, usually by postsynaptic scaling [6]. A stable state of activity requires a balance between excitation and inhibition. Since network topology is subject to constant change, some form of stabilizing, homeostatic feedback control has to be implemented in order to maintain this equilibrium. While recent theoretical studies have also argued that stabilization of recurrent networks could be achieved by the presence of inhibitory plasticity [7], common forms of homeostasis are believed to take place either through the modulation of excitatory synapses [8], or by modifications of intrinsic neuronal excitability [9]. Previous research on a binary self-organizing recurrent neural network (SORN) by Lazar et al. [1] and a more biologically realistic spiking version of this network (LIF-SORN) by Miner and Triesch [10] used an intrinsic homeostatic control mechanism to regulate excitatory activity on a single-cell level. Despite this very simple form of homeostatic control, the network has proven to be capable of showing a number of experimentally confirmed non-random features. Zheng et al. have shown that the distribution and dynamics of synaptic efficacies measured in rat hippocampi can be reproduced by a binary SORN using a discretized version of spike-timing-dependent plasticity and presynaptic normalization [11]. With the LIF-SORN, Miner et al. reproduced the results of the binary SORN regarding self-organizing synaptic dynamics. Furthermore, they were able to explain the experimentally observed overrepresentation of bidirectional connections [12,13] by means of a distance-dependent implementation of synaptic growth. Furthermore, so-called *triadic motifs*, which subsume possible connectivity patterns between triplets of neurons, have been found to be significantly overrepresented compared to chance, if a combination of STDP and a distance-dependent connectivity profile was used. The SORN's ability of self-organization has not only been investigated in terms of network structure itself. It also successfully performed in unsupervised sequence-learning tasks, suggesting that it can acquire and maintain associative memory [14].

As mentioned above, previous versions of our recurrent network model regulated activity by fixing excitatory firing rates to a predefined target value. However, strong evidence exists for a log-normal like distribution of cortical firing rates [15,16]. Experimental and theoretical studies have suggested that the presence of both slow- and fast-firing cells is not to be regarded as an ignorable, mere side effect of brain dynamics [17–19]. It rather seems to be that skewed and heavy-tailed firing rate statistics are necessary with respect to the preservation of stable synaptic structures being related to long-term memory, while still allowing synaptic rewiring in order to adapt to changes in external stimuli [15]. A realistic network model of neural activity and plasticity should therefore allow for a broad distribution of firing rates to cope with

Table 1. Parameters of synaptic connections.

parameter	EE	EI	IE	II
connection fraction	→ 0.1	0.1	0.1	0.5
initial connection strength	0.0001 mV	1.5 mV	−1.5 mV	−1.5 mV
conduction delay	1.5 ms	0.5 ms	1.0 ms	1.0 ms

these functional aspects.

In this paper we examine *diffusive homeostasis* as a possible candidate to replace a previously used model of single-cell intrinsic plasticity. The idea and modeling of diffusive homeostasis was adopted from a paper by Sweeney et al. [20], which models neural tissue as a two-dimensional surface and a set of points representing the neurons' positions. The group of excitatory neurons acted as a point-source of nitric oxide (NO) as well as as a sensor for the NO concentration at each individual position. The production and sensing of NO forms the basis of a feedback loop: The individual NO readout is fed into a comparator which causes an appropriate change within the internal firing threshold of the neuron, in turn altering the neuron's firing rate. The control system is then closed by linking the rate of NO production to the neuron's firing rate. The results by Sweeney et al. suggest that diffusive signaling could resolve the dichotomy between overall stability of firing activity and the need to allow flexibility among individual neurons' activities. Through the diffusive signal, each neurons receives - intuitively speaking - a mixture of its own activity and its neighboring neurons. Individual tuning of firing rates is thereby suppressed while the overall population activity is kept at a constant level.

Key aspects of this paper include an analysis of the stability of the homeostatic control, followed by a comparison of features of the original LIF-SORN and the diffusive variant. We expected to observe a preservation of non-random features that have been found in the original LIF-SORN while incorporating a stronger variance within neural activity which has previously been suppressed by single-cell homeostasis. Furthermore, we predicted excitatory activity on the level of individual cells by an analytic approach, thereby gaining an understanding of the relation between spatial structure and firing rates. In the face of possible new features within the network's structure, we clarify the causal relation between diffusive spatial interaction and synaptic topology.

Materials and methods

Network simulation

400 excitatory LIF neurons and 80 inhibitory LIF neurons were assigned random positions across a square area of $1000 \times 1000 \mu\text{m}$. All except recurrent excitatory synapses were randomly generated before the start of the simulation until a desired connection fraction was reached. The connection probability between two neurons was calculated from a distant dependent Gaussian function with a standard deviation of $200 \mu\text{m}$. For excitatory to inhibitory (EI) and inhibitory to excitatory (IE) synapses, the connection fraction was set to 0.1, and 0.5 for recurrent inhibitory synapses (II). These connections were kept at a fixed connection strength throughout the simulation. Furthermore, all synapses were simulated with a fixed (distance independent) conduction delay. See Table 1 for a summary of parameters.

Recurrent excitatory synapses were subject to a number of plasticity mechanisms to be described in the following.

Synaptic plasticity

Synaptic Growth: New synapses are generated at an average rate of 920 per second. For efficiency, this was implemented by drawing an integer number from a normal distribution with mean 920 and standard deviation $\sqrt{920}$ once per second and simultaneously inserting this number of synapses. This growth rate was tuned to achieve the desired target concentration of 0.1 (see Table 1).

Synaptic Pruning: The process of synaptic pruning was similarly carried out by checking for EE synapses below a threshold of 10^{-6} mV once each second (same instant as growth) and removing them simultaneously, and thus adding them again to the set of “potential” connections from which the growth process draws new connections.

Spike Timing Dependent Plasticity: An additive STDP rule was used as described e.g. in [5]. The change of weight between two neurons due to a pre- and postsynaptic spike ($i \rightarrow j$) is defined as:

$$\Delta w_{ji} = \sum_k \sum_l W(t_j^l - t_i^k) \quad (1)$$

$$W(\Delta t) = A_+ \exp(-\Delta t / \tau_+), \quad \Delta t \geq 0 \quad (2)$$

$$W(\Delta t) = A_- \exp(\Delta t / \tau_-), \quad \Delta t < 0 \quad (3)$$

Indexes k and l refer to the k -th and l -th pre- and postsynaptic spike respectively. Parameters were chosen to approximate data from [21] and [22], namely $\tau_+ = 15$ ms, $A_+ = 15$ mV, $\tau_- = 30$ ms and $A_- = -7.5$ mV. However, we used the “nearest neighbor” approximation for the sake of reduction of computational effort, only calculating the effect of the most recent pre-post pair of spikes for potentiation and post-pre pair for depression, yielding roughly the same value as the full summation due to the fast decay times τ_+ and τ_- of the STDP-window.

Synaptic Normalization: For the same reasons of efficiency, synaptic normalization was applied at the same rate as synaptic growth/pruning, updating each w_{ji} from neuron i to neuron j as follows:

$$w_{ji} \rightarrow w_{ji} \frac{w_{\text{total}}}{\sum_i w_{ji}} \quad (4)$$

w_{total} was set to different values for each of the four types of connections between the excitatory and inhibitory pool of neurons. Except for the dynamically populated EE-synapses these values could be directly set in accordance with the previously given parameters of desired mean individual connection strength, size of the presynaptic population and connection fraction, by calculating $w_{\text{total}} = w_{\text{mean}} N_{\text{presyn}} p_{\text{conn.}}$, where w_{mean} is given by the initial synaptic strength in Table 1, $N_{\text{presyn.}}$ is the number of neurons and $p_{\text{conn.}}$ is the synaptic connection probability given in Table 1. This yielded $w_{\text{total, EI}} = 60$ mV, $w_{\text{total, IE}} = -12$ mV, $w_{\text{total, II}} = -60$ mV. $w_{\text{total, EE}}$ was set to 40 mV, corresponding to a mean synaptic weight of 1 mV, given a targeted EE-connection fraction of 0.1 and a population of 400 excitatory neurons.

Short Term Plasticity: A short term plasticity (STP) mechanism acting on recurrent excitatory connections was implemented as presented in [23] as an additional stabilization of network activity. It modulates the effective synaptic weights by multiplying the value stored in the weight matrix w_{ji} by two dynamic variables x and u , $w_{ji}^{\text{effective}} = w_{ji} \cdot x \cdot u$, each synapse owning a pair (x, u) . The dynamics of these variables are given by:

$$\dot{x} = \frac{1-x}{\tau_d}, \quad \dot{u} = \frac{U-u}{\tau_f} \quad (5)$$

Table 2. Parameters of LIF neuron.

parameter	exc. neur.	inh. neur.
E_l	−60 mV	−60 mV
τ_m	20 ms	20 ms
V_r	−70 mV	−60 mV
σ	$\sqrt{5}$ mV	$\sqrt{5}$ mV
V_t	subject to IP	−58 mV

Each presynaptic spike furthermore causes a change of x and u by

$$x \rightarrow x - x \cdot u, u \rightarrow u + U(1 - u) \quad (6)$$

We chose $U = 0.04$, $\tau_d = 0.5$ s and $\tau_f = 2$ s as a rough approximation of the values that were experimentally observed [23]. For our choice of variables, a Poisson input with a constant rate achieves the best synaptic transmission at a rate of ~ 4.5 Hz, corresponding to $x \cdot u \approx 0.2$. *Potentiation* in this context refers to the fact that stronger input strengthens synaptic transmission compared to close to zero incoming spikes.

Neuron model

We used a leaky integrate-and-fire-model with a simple additive synaptic transmission model for all neurons in the network, whose dynamics are described by a stochastic differential equation:

$$\tau_m dV_i = -(V_i - E_l) dt + \sqrt{\tau_m} \sigma dW_i + \tau_m \sum_{j,k} w_{ij}^{\text{effective}} \delta(t_{\text{spike},j}^k + t_{\text{delay}} - t) \quad (7)$$

where V is the membrane potential, E_l is the equilibrium membrane potential, τ_m is the membrane time constant, σ is the standard deviation of the noise term and dW is the standard Wiener process. A neuron is generates a spike when its membrane potential reaches the threshold voltage V_t . The voltage is then reset to V_r . A refractory period was not implemented. A presynaptic spike causes a simple (delayed, see Table 1) increment of the membrane potential of the postsynaptic neuron by $w_{ji}^{\text{effective}}$. Table 2 summarizes the aforementioned set of parameters.

Intrinsic plasticity

Apart from dynamic processes within synapses which contribute to a stabilization of the network's activity, neurons possess internal mechanisms capable of maintaining a desired regime of activity. Regular-spiking cells are known to down-(up-)regulate their firing rate upon increased (decreased) input on a timescale of tens of milliseconds [24, 25]. The network itself was not expected to exhibit fast changes of synaptic input since our simulation did not incorporate any rapidly changing external drive, which allowed us to neglect this feature. On the other hand, a similar form of adaption as a reaction on deprived or enhanced input can be observed on a timescale of hours to days [26]. In the latter case, a long-term change in excitability can be attributed to an altered number of permeable ionic channels. This contrasts the former short-term adaption, which can be explained by a separation of timescales among different ionic currents in the cell. A simple form of low intrinsic homeostasis was implemented in the original LIF-SORN by altering the neurons' firing threshold based on the deviation from a target firing rate. During the research reported by this paper, we implemented a new model of slow intrinsic homeostasis, based on the work presented in [20]. The following section describes both models in further detail.

Our original model of homeostatic control was described by the following differential equation:

$$\dot{V}_t = \eta_{IP}(r - r_{IP}) \quad (8)$$

with r as the neuron's firing rate and r_0 the target firing rate, η_{IP} the rate of threshold adaptation and r the estimated firing rate of a single excitatory neuron. In practice, this was implemented in discrete steps of $\Delta t = 0.1$ ms, estimating the firing rate by $r = N_{\text{spikes}}/\Delta t$, with N_{spikes} as the number of spikes within each interval.

The new diffusive homeostatic model by Sweeney et al. consists of a set of differential equations:

$$[\text{Ca}^{2+}]_i(t) = -\frac{[\text{Ca}^{2+}]_i}{\tau_{\text{Ca}^{2+}}} + Ca_{\text{spike}}^{2+} \sum_j \delta(t - t_{\text{spike},i,j}) \quad (9)$$

$$[\text{nNOS}]_i(t) = \frac{1}{\tau_{\text{nNOS}}} \left(\frac{[\text{Ca}^{2+}]_i^3}{[\text{Ca}^{2+}]_i^3 + 1} - [\text{nNOS}]_i \right) \quad (10)$$

$$[\dot{\text{NO}}](\mathbf{r}, t) = -\lambda[\text{NO}] + D\nabla^2[\text{NO}] + \sum_i \delta^2(\mathbf{r} - \mathbf{r}_{\text{neur},i})[\text{nNOS}]_i \quad (11)$$

$$\dot{V}_{t,i}(t) = \frac{[\text{NO}](\mathbf{r}_{\text{neur},i}, t) - [\text{NO}]_0}{NO_0 \tau_{V_i}} \quad (12)$$

A depolarization within a nerve cell upon a spike-event t_{spike} causes a fixed inflow of ionic current Ca_{spike}^{2+} , which is modeled as an instantaneous increase of the $[\text{Ca}^{2+}]$ concentration. The concentration decays exponentially by a time constant $\tau_{\text{Ca}^{2+}}$. Though Ca^{2+} currents can be described in a much more detailed fashion, it can be considered as a reasonable approximation [27, p. 198-203]. The influence of $[\text{Ca}^{2+}]$ onto $[\text{nNOS}]$ was modeled by Sweeney et al. through (10) using the Hill equation [28] to model a cooperative binding mechanism. The rate of $[\text{nNOS}]$ is then fed into the “pool” of nitric oxide via point sources located at the neurons' positions. An additional decay term was added apart from the inflow and the diffusive term to provide a stable finite $[\text{NO}]$ concentration under constant neuronal activity.

Finally, the dynamics of firing thresholds $V_{t,i}$ were modeled such that the rate of change is proportional to the relative deviation of NO concentration at the neurons' locations from a global target concentration $[\text{NO}]_0$.

To acquire a target concentration $[\text{NO}]_0$ corresponding to the desired mean firing rate, we let the system run with the previous homeostatic mechanism, still solving Eq. (9)-(11) until a steady mean over the concentrations at the neurons' positions was reached. This mean was then set to be the target concentration and we switched to diffusive homeostasis. Table 3 summarizes the choice of parameters that were introduced in this section. Diffusion parameters roughly match those measured in experiments [29].

Simulation of diffusion

We solved (11) with the finite difference method on a grid $\mathbf{r}_{i,j}$ with a resolution of 100×100 points. Integration over time was carried out by a 4th-order Runge-Kutta method with a time step of 1 ms. $\nabla^2 \text{NO}(\mathbf{r}_{i,j}) = \nabla^2 \text{NO}_{i,j}$ was approximated by

$$\nabla^2 \text{NO}_{i,j} \approx \frac{\text{NO}_{i+1,j} + \text{NO}_{i-1,j} + \text{NO}_{i,j+1} + \text{NO}_{i,j-1} - 4\text{NO}_{i,j}}{h^2} \quad (13)$$

on each time step, where $h = L/100$ is the distance between neighboring grid points, determined by the length L of the square sheet and the resolution of the numeric grid. We implemented three possible boundary conditions:

Table 3. Parameters of homeostatic intrinsic plasticity.

parameter	value
r_{IP}	3 Hz
η_{IP}	0.1 mV
Ca_{spike}^{2+}	1
$\tau_{Ca^{2+}}$	10 ms
τ_{nNOS}	100 ms
D	default: $10 \mu m^2 ms^{-1}$
λ	$0.1 s^{-1}$
τ_{V_t}	2500 s

1.) Periodic boundary conditions:

$$NO_{i,N_{grid}} = NO_{i,0} \quad (14)$$

$$NO_{N_{grid},i} = NO_{0,i} \quad (15)$$

$$NO_{i,-1} = NO_{i,N_{grid}} \quad (16)$$

$$NO_{-1,i} = NO_{N_{grid},i} \quad (17)$$

with N_{grid} being the grid resolution.

2.) Neumann boundary conditions with $\nabla NO = (0, 0)$ at the boundaries:

$$NO_{i,N_{grid}} = NO_{i,N_{grid}-2} \quad (18)$$

$$NO_{N_{grid},i} = NO_{N_{grid}-2,i} \quad (19)$$

$$NO_{i,-1} = NO_{i,1} \quad (20)$$

$$NO_{-1,i} = NO_{1,i} \quad (21)$$

3.) Dirichlet boundary conditions with $NO = NO_{bound.}$ at the boundaries.

Neumann boundary conditions were used for most of the simulations if not explicitly stated otherwise. This decision relates to the previously described mechanism of synaptic growth: Neurons placed close to the edge of the sheet have a lower connection probability due to the absence of neighboring neurons in the direction perpendicular to the close-by border. It therefore models the synaptic growth within a square “cutout” of neural tissue. The Neumann boundary condition fits into this picture since it allows a zero-flux condition at the borders. This is a reasonable assumption, because NO molecules cannot diffuse out of the tissue (unless they were placed in a surrounding fluid).

Eq. (11) describes the influx of [NO] as a sum of scaled and spatially shifted Dirac functions. Apart from the question whether this source term results in a well defined, finite analytic solution at the neurons’ positions (see Section *Spatial configuration of neurons allows for the precise prediction of firing rates*), it can only be modeled to a certain degree of accuracy depending on the resolution of the numeric grid. In practice, we approximated the point sources of NO as insertions at individual grid cells at a rate of $[nNOS]_i(t)/h^2$, where the normalizing divisor h^2 ensured the desired total influx per neuron. This numeric implementation required two additional constraints: First, all random neuron positions were confined to integer multiples of h in x- and y-direction. Second, to avoid redundancy and for physiological reasons, each grid cell could only hold one neuron at maximum.

Software

The Neural Network was simulated in python using the BRIAN spiking neural network simulator package [30]. Plots were generated using the Matplotlib python package [31].

Table 4. Diffusion constants and number of simulations used in Fig. 1E and F.

D [$\mu\text{m}^2\text{ms}^{-1}$]	Number of Sim.
0.0	1
0.1, 0.2, ..., 0.8, 0.9	2
1.0, 2.0, ..., 5.0, 8.0, 10.0, 15.0, 20.0	4

Results

Distribution of firing rates

Fig. 1A–D shows a first result for the distribution of firing rates, comparing both homeostatic mechanisms. As expected, non-diffusive homeostasis led to a sharp distribution of firing rates at 3 Hz. Diffusive homeostasis indeed resulted in a much broader distribution of mean firing rates. In panel A, we found a skewness of $v_{\text{diff.}} = 0.765$ for diffusive homeostasis. To assess whether the statistics resemble a log-normal distribution, we also plotted the distribution of decadic logarithms of firing rates in Fig. 1B and D and compared it to a normal distribution. Panel B shows the distribution of the decadic logarithms of excitatory firing rates. The fact that the distribution is well fit by a normal distribution indicated that firing rates were indeed approximately log-normal distributed. Excitatory firing rates were relatively unaffected by changing the homeostatic mechanism, see panels C and D.

Sweeney et al. found that diffusive homeostasis maintains the broadness of the distribution of firing rates across a wide range of diffusion constants but rapidly approaching zero for small values (cf. [20], Fig. 3C). We were able to reproduce this result, see Fig. 1E. Homeostasis reaches a point of saturation, where faster diffusion has no effect on the heterogeneity of firing rates. Each of the data points in Fig. 1E and F corresponds to a single full simulation, though the same simulation data was used in A and B. 55 simulations were run in total. We picked the D-values by hand to achieve a good representation of the overall trend while limiting the amount of simulations. The set of diffusion constants used is given in Table 4. We also investigated the influence of the diffusion constant onto the distribution's skewness, shown in Fig. 1F, to further quantify this dependence. Compared to the standard deviation, we saw a similar but not as clear trend with a drop for very small diffusion constants, even occasionally resulting in a left-skewed distribution (negative D-values).

A naturally emerging question when altering the diffusion constant is how excitatory firing rates behave in the absolute limit of infinitely fast diffusion. In fact, this case is quite easy to implement in the simulation: One simply has to feed all NO sources into a single scalar variable of NO concentration. This then provided the same NO readout for all excitatory neurons, which means that all excitatory thresholds changed at the same rate all the time, only shifting their initial distribution. Therefore, the effect of this particular distribution will remain present for the entire simulation, and a larger variance among excitatory thresholds will likely also broaden the distribution of firing rates. However, we chose to set all excitatory thresholds to the same initial value. Fig. 1A–D shows the distributions for this case. As one can see, this results in a similar but broader log-normal like distribution of excitatory firing rates, going along with a more pronounced skewness ($v_{\text{inst.diff.}} = 1.51$).

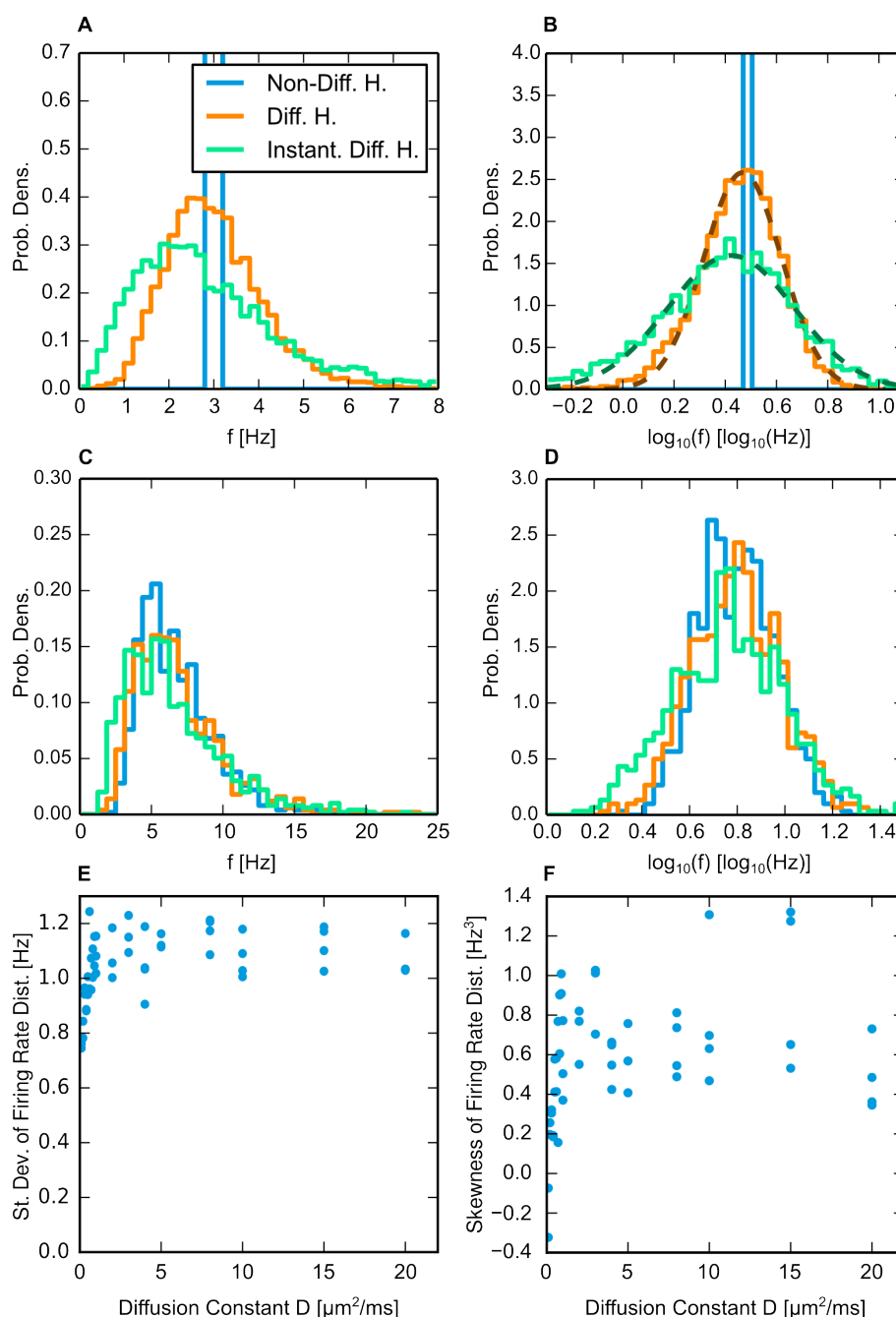


Fig 1. Distribution of firing rates. A,B,C,D: Histograms of mean firing rates over the excitatory (A/B) and inhibitory (C/D) population in regular (A/C) and logarithmic space (B/D). Distributions were generated from 10 simulation runs, 1 simulation was used for non-diffusive homeostasis. Mean firing rates were calculated from spikes within $1000 \text{ s} \leq t \leq 1500 \text{ s}$. E,F: Standard deviation (E) and skewness (F) of firing rate distribution of excitatory neurons (Neumann boundary conditions). Each data point was generated from one full simulation.

Previously reported features of network topology and dynamics are preserved

While we explicitly intended altering the statistics of excitatory firing rates by implementing diffusive homeostasis, we hoped to preserve what has previously been reported by Miner and Triesch regarding the evolution and structure of recurrent excitatory weights [10]. Fig. 2 summarizes features that we found to be preserved for diffusive homeostasis. Diffusive homeostasis leads to the same stable level of recurrent excitatory connection fraction, as well as the observation that a non-uniform connection profile is required to allow for an over-representation of bidirectional connections, as reported previously [10]. A more general discussion on this issue was given by Hoffmann and Triesch [32]. Fig. 2,C shows that a log-normal like distribution of excitatory weights is preserved under diffusive homeostasis. Fig. 2 D illustrates the preservation of a power-law distribution of recurrent excitatory synaptic lifetimes during the steady phase of connectivity. Given the assertion that the slope of this distribution is linked to the overall balance of synaptic potentiation and depression [10], we can assume that both types of homeostasis result in a similar net difference between potentiation and depression. Fitting of the power-law exponent was done with the *powerlaw python package* [33], which used a maximum-likelihood method to fit power-law exponents to the lifetime data.

Heterogeneity of firing rate leads to the emergence of strongly influential excitatory neurons

Having reproduced these results of the previous model, we further sought for possible differences within our network topology as a result of diffusive homeostasis. Since we only implemented synaptic normalization for the sum of ingoing weights, the total or average strength of *outgoing* connections may vary from cell to cell. In a sense, the strength of outgoing connections per neuron can be regarded as a measure of how influential a neuron's activity is with respect to other neurons in the network. Effenberger et al. have shown in computational studies that these "driver neurons" form highly active and interconnected subnetworks [4], an observation that is backed up by experimental studies [34,35]. Fig. 3A shows that diffusive homeostasis allows for the emergence of a small group of highly influential neurons, which resembles the findings in [4]. A comparison of statistics generated with shuffled versions of the weight matrices illustrates that above-chance exceptionally strong mean outgoing weights were indeed present. Statistical significance of the differences depicted in Fig. 3A was additionally tested by means of a two-sample Kolmogorov-Smirnov test, yielding p-values of $< 10^{-30}$ for all non-identical sets of weights.

Synapses between highly active presynaptic cells and postsynaptic neurons with lower activity are known to be subject to long-term potentiation [36,37]. With this causal relations in mind, we can argue that diffusive homeostasis effectively embodies a similar functional role as inhibitory STDP in [4] by allowing for the presence of excitatory cells with above-average activity. We tested this relationship by plotting the mean outgoing weights against the average firing rate, see Fig. 3C/D. A strong heterogeneity of firing rates allowed for the development of few neurons with comparably strong mean outgoing weights, while the distribution of mean weights resulting from a narrow distribution is limited to a smaller range. We also tested the case of instantaneous diffusion. Though firing rates spanned across a similar range, mean weights did not reach as high values as in the case of diffusion at a finite rate.

Experimental studies have not only considered the presence of neurons with strong influence onto other neurons [35], but also found evidence that highly active neurons form subnetworks with an increased connectivity, in the sense that these cells are more

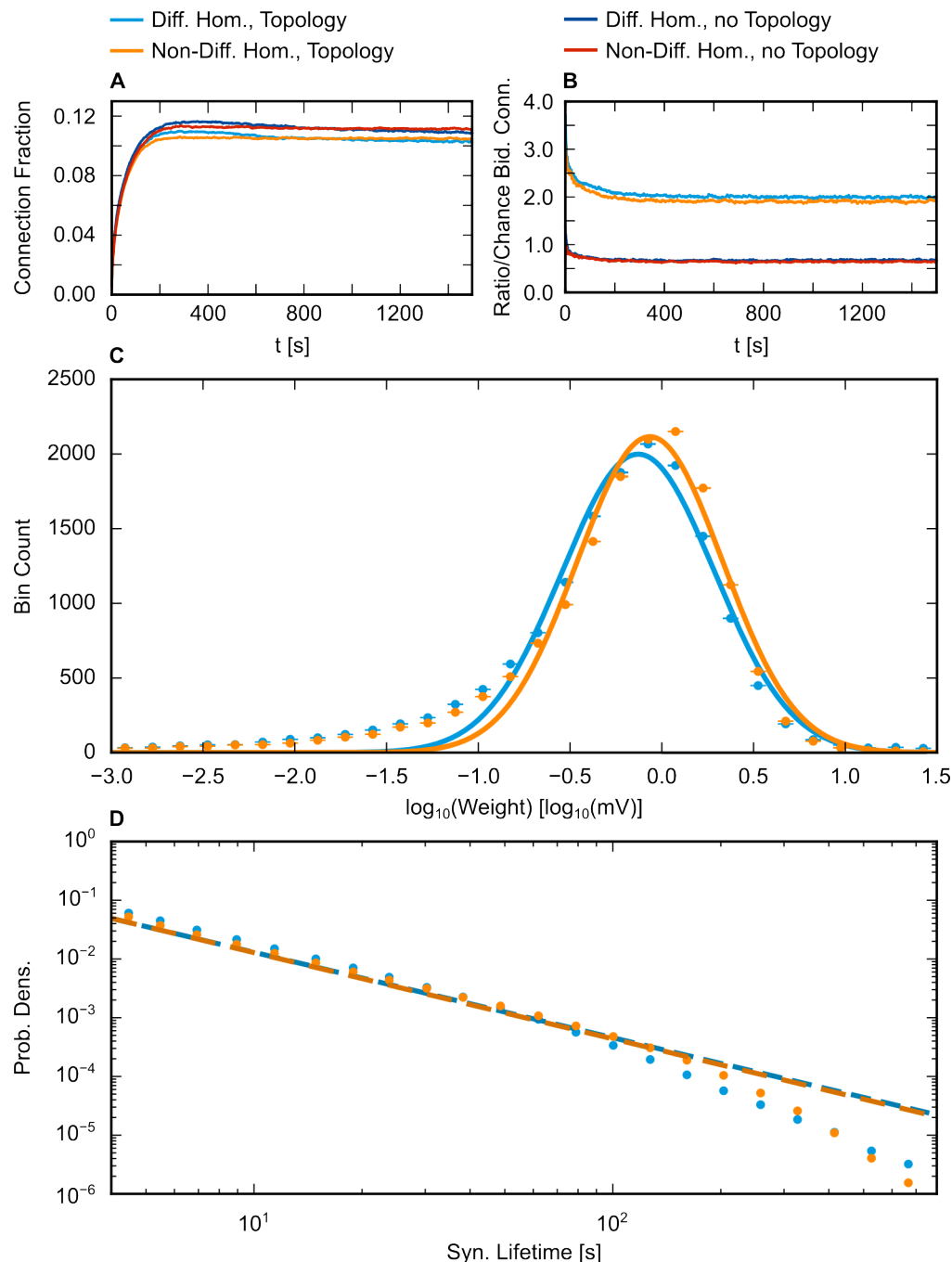


Fig 2. Time course of recurrent excitatory connection fraction. **A:** Evolution of recurrent excitatory connection fraction. *Topology* refers to the presence or absence of a Gaussian connection profile. **B:** Ratio of bidirectional connections relative to a random Erdős-Rényi graph. **C:** Distribution of excitatory recurrent weights after 1500 s. Solid curves are Gaussian fits. Data was taken from 5 simulations. **D:** Distribution of recurrent excitatory synaptic lifetimes. Single-trial data. Solid lines are estimates of a power-law exponent, giving a slope of approximately -1.9 for diffusive homeostasis and -1.7 for non-diffusive homeostasis. 5 simulation runs were used for each curve in panels A and B, panels C and D show representative single-trial data.

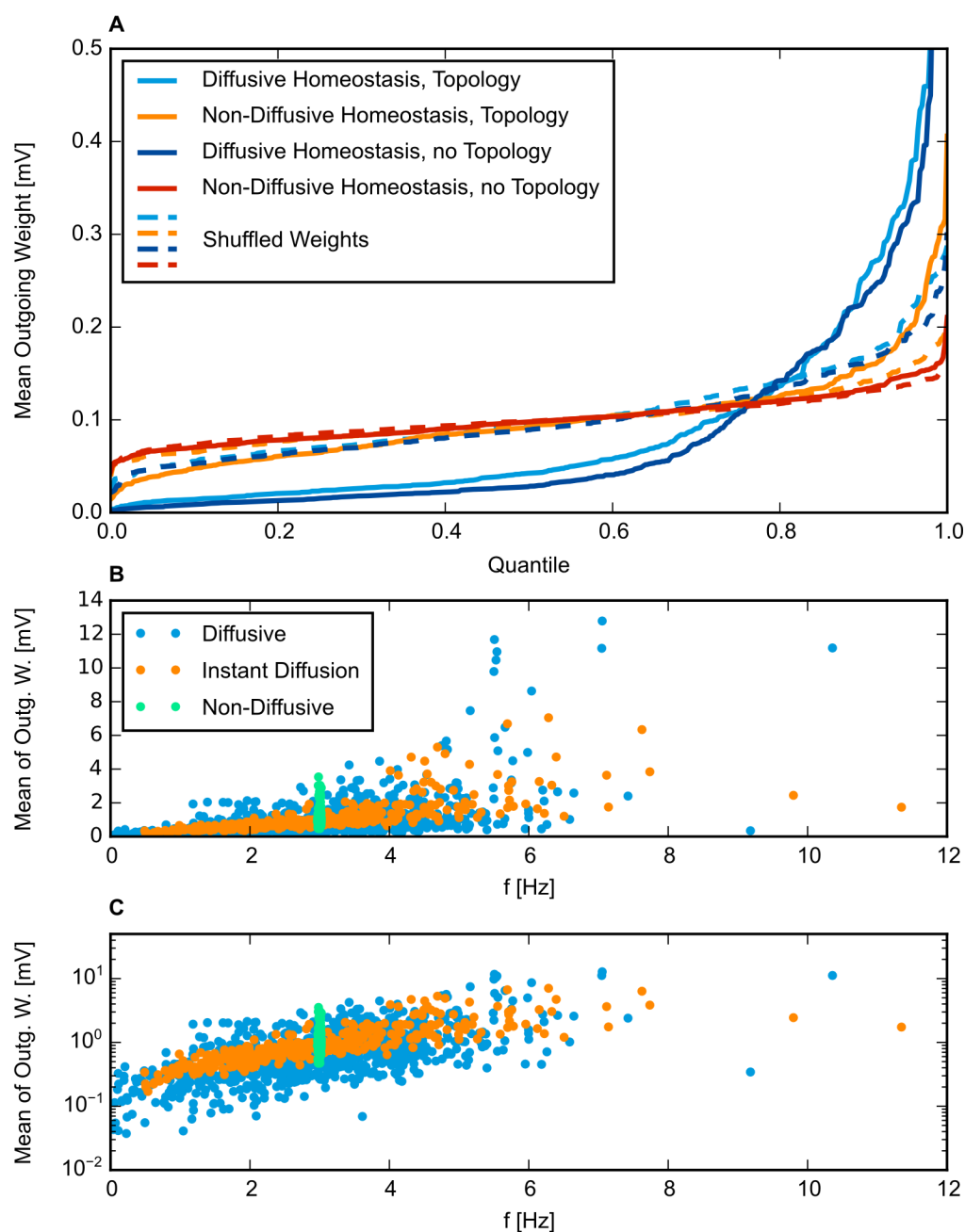


Fig 3. Quantile function of mean excitatory outgoing weights. **A:** Mean of outgoing weights of excitatory neurons in order sorted by magnitude. Dashed lines are means obtained by randomly shuffling synaptic weights. Data was taken from 25 weight matrices per line, representing weights within $1000\text{ s} \leq t \leq 1500\text{ s}$. **C/D:** Mean of outgoing excitatory weights at $t = 1500\text{ s}$ plotted against mean presynaptic firing rate (averaged over $700\text{ s} \leq t \leq 1000\text{ s}$) in regular (**C**) and logarithmic space (**D**). Each plot corresponds to a presynaptic excitatory cell. Two simulation runs were used for diffusive homeostasis, all other are single-trial data.

likely than average to connect to each other, see [34]. We tested this in our network by evaluating the connection fraction $CF_{diff.,leader}$ among the top 10% of excitatory neurons with respect to their average firing rate within $1000s \leq t \leq 1500s$ and comparing it to the rest of the excitatory population and the same calculation for the non-diffusive case. This returned $CF_{diff.,leader} = 0.1371 \pm 0.0061$, $CF_{diff.,non-leader} = 0.0982 \pm 0.0013$, $CF_{non-diff.,leader} = 0.0954 \pm 0.0044$ and $CF_{non-diff.,non-leader} = 0.0992 \pm 0.0002$. Standard errors were calculated from 5 simulation runs for each homeostatic mechanism, and connectivity matrices were taken from $t = 1500s$. This showed that connectivity is indeed increased among the fastest-firing 10% of the neurons in the case of diffusive homeostasis. Effenberger et al. reported a similar effect, in fact with even more pronounced differences of connectivity [4].

Spatial configuration of neurons allows for the precise prediction of firing rates

Having analyzed the distribution of firing rates resulting from the implementation of diffusive homeostasis, we were interested in how strongly the actual positioning of excitatory neurons influences the resulting statistics of firing activity. To do so, we assumed that the spontaneous firing measured during the stable phase of the network, characterized by a constant excitatory connectivity, can be regarded as a homeostatic steady state. Given no sudden strong changes of neural input, the homeostatic feedback levels out the error to approximately zero, since Eq. 12 is a realization of an integral control. Our search for the steady-state configuration of firing rates thus reduced to finding a set of firing rates that led to a concentration level of NO_0 at every excitatory neuron's position:

$$NO(\mathbf{x}_{neur.,i}) = NO_0, \forall i. \quad (22)$$

Furthermore, we found that the nonlinearity between spiking activity and NO synthesis could be well approximated by a linear relation between average firing rate r_i and rate of NO synthesis $nNOS_i$ by

$$nNOS_i = \frac{Ca^{2+3}_{spike} \tau_{Ca^{2+}} \ln(2)}{3} \cdot r_i \equiv \gamma r_i. \quad (23)$$

See Appendix S1 for a derivation of the proportionality factor. Given this simplification, the steady state of NO concentration is thus defined by the solution of

$$0 = -\lambda NO + D \nabla^2 NO + \sum_i \delta^2(\mathbf{x} - \mathbf{x}_{neur.,i}) \cdot \gamma \cdot r_i \quad (24)$$

$$\left(\nabla^2 + \left(i \sqrt{\frac{\lambda}{D}} \right)^2 \right) NO = \sum_i \delta^2(\mathbf{x} - \mathbf{x}_{neur.,i}) \cdot \frac{-\gamma \cdot r_i}{D} \quad (25)$$

which is a two-dimensional Helmholtz equation. Its Green's function is

$$NO(\mathbf{x}) = \frac{r_i \gamma}{2\pi D} K_0 \left(|\mathbf{x}| \sqrt{\frac{\lambda}{D}} \right) \equiv r_i \cdot \psi_{point}(|\mathbf{x}|) \quad (26)$$

where K_0 is the zeroth modified Bessel function of the second kind [38]. This solution reveals a fundamental problem of modeling the sources of NO production as point sources: the fact that $K_0(\mathbf{x})$ diverges to infinity for $\mathbf{x} \rightarrow 0$. It is merely due to the finite density of the numeric grid used for the simulation of diffusion that allows for a finite target value of concentration.

Generally speaking, no matter how the actual shape of the numeric solution in the equilibrium at a constant production rate looks like, it must be of the form

$$NO_i(\mathbf{x}) = r_i \cdot \psi(|\mathbf{x}_{\text{neur},i} - \mathbf{x}|) . \quad (27)$$

The full solution is then

$$NO(\mathbf{x}) = \sum_i NO_i(\mathbf{x}) . \quad (28)$$

By defining

$$\psi_{ij} \equiv \psi_{ij} \equiv \psi(|\mathbf{x}_{\text{neur},i} - \mathbf{x}_{\text{neur},j}|) \quad (29)$$

we could express condition (22) as

$$\sum_j \psi_{ij} \cdot r_j = NO_0 \quad (30)$$

or, as an operator

$$\hat{\psi} \mathbf{r} = NO_0 \mathbf{n} \quad (31)$$

$$\mathbf{n} \equiv (1, 1, \dots, 1) . \quad (32)$$

The problem of finding the steady-state solution of the homeostatic constraint thus reduced to inverting $\hat{\psi}$:

$$\mathbf{r} = NO_0 \hat{\psi}^{-1} \mathbf{n} \quad (33)$$

Still, we had to find a modified, non-diverging version of $\psi(d(\mathbf{x}_{\text{neur},i}, \mathbf{x}))$ to acquire any prediction from this model. It had to retain the shape given by (26) for larger distances but approach the correct numeric error value at the origin, determined by the spacing of the numeric grid. We solved this problem by the following expression:

$$\psi_{\text{approx.}} \equiv \frac{1}{\left(\frac{1}{\psi_0^\varepsilon} + \frac{1}{\psi_{\text{point}}^\varepsilon} \right)^{\frac{1}{\varepsilon}}} \quad (34)$$

where ε determines the “smoothness” of transition between ψ and the cutoff value ψ_0 . We chose $\varepsilon = 10$ for all further calculations. We took the simple approach of interpreting this value as a mean of the analytic solution across the area covered by the corresponding grid cell to find an expression for ψ_0 . As an additional simplification, we substituted the necessary integration over the square grid cell by a circular area of equal size around the source. This calculation yielded

$$\psi_0 = \gamma \frac{1 - h \sqrt{\frac{\lambda}{\pi D}} K_1 \left(h \sqrt{\frac{\lambda}{\pi D}} \right)}{h^2 \lambda} \quad (35)$$

where h is the spatial resolution of the grid cells.

By simply calculating all matrix elements of $\hat{\psi}$ by means of Eq. (29), one would neglect the finite boundaries of the system, which would cause neurons close to the edge to “bleed” into empty space. We accommodated for zero-flux Neumann boundary conditions by adding appropriately mirrored copies of the neurons’ positions, canceling the orthogonal component of the gradient at the boundaries.

After having worked out the analytical basis, we compared the prediction obtained from numerically solving Eq. (31) for certain spatial configurations of neurons to the steady-state firing rates of the full spiking network with the same spatial structure. We were particularly interested in the quality of the predictions with respect to the choice of diffusion constant. Fig. 4B shows three examples: For $D = 10 \mu\text{m}^2\text{ms}^{-1}$, the

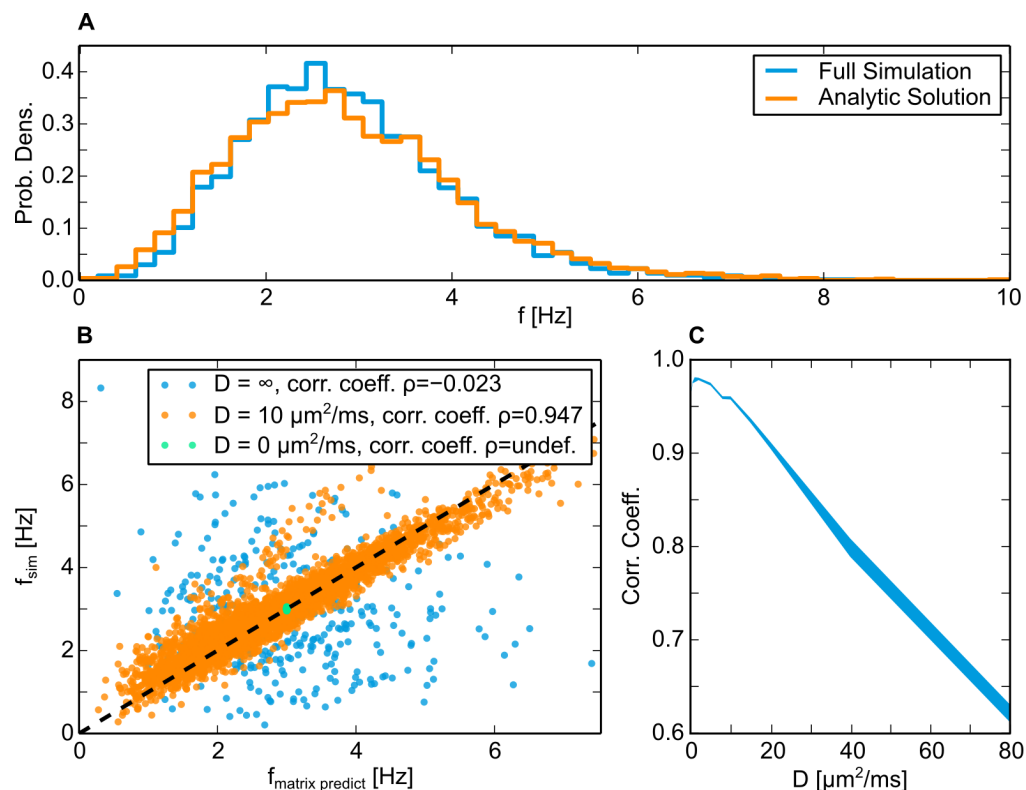


Fig 4. Empirical distribution of excitatory firing rates and theoretical prediction. **A:** Distribution of firing rates for $D = 10 \mu\text{m}^2\text{ms}^{-1}$, full simulation and analytic prediction. Data was taken from 10 simulation runs. **B:** Measured firing rates ($1200\text{ s} \leq t \leq 1500\text{ s}$) versus predicted firing rates based on the solution of Eq. (31). For $D = \infty$ (instantaneous diffusion in the full simulation), the analytic prediction was calculated with a comparably large diffusion constant of $D = 100 \mu\text{m}^2\text{ms}^{-1}$. Plot shows representative single-trial data. **C:** Pearson correlation coefficient of predicted and measured firing rates (see Panel C) versus diffusion constant. Line width depicts standard error, 5 simulations were used for each D -value.

correlation between measured and predicted firing rates is very good. In contrast, we included the - obviously unsuccessful - attempt to predict firing rates for a simulation with instantaneous diffusion based on the spatial structure by setting D to a relatively high value of $D = 100 \mu\text{m}^2\text{ms}^{-1}$. This represented a limiting case where our analytic model could not make any meaningful predictions, since instantaneous diffusion overrides any spatial inhomogeneities. The outcome of the third case shown in the plot, $D = 0$, is correctly predicted by the analytic model. In general, instantaneous diffusion as well as $D = 0$ overrode the effects of spatial heterogeneity onto firing rates. As Fig. 4A shows, the actual shape of the distribution was also well predicted by the solution of the linear system.

These observations naturally led us to the question of how the correlation between predicted measured firing rates behaves in between the aforementioned limits. Especially, we were interested in the range of the diffusion constant for which our model provides a good description of the full spiking network's activity. Fig. 4C depicts the Pearson correlation coefficient of $f_{\text{matrix,predict}}$ and f_{sim} against the diffusion constant used in the simulation. A relatively high correlation was obtained for a wide range of

diffusion constants. However, we could see a general decline of correlation for larger diffusion constants. This trend was in line with the aforementioned limit of instantaneous diffusion, namely a complete decorrelation between prediction and measurement, as well as the good agreement for $D = 10 \mu\text{m}^2\text{ms}^{-1}$ shown in Fig. 4A.

Having acknowledged the good agreement between the full network simulation and the predictions of our simplified model, we also made predictions for more realistic settings of spatial densities. Although neuronal densities can vary considerably across different cortical areas and species [39], we considered a density of $9 \cdot 10^4 \text{mm}^{-1}$ as a realistic value [40]. This corresponds to a mean free path of $22.31 \mu\text{m}$. On a single two-dimensional slice of $1000 \times 1000 \mu\text{m}$, one should therefore populate approximately 2000 neurons to achieve the same mean free path. For the sake of a larger sample set, we calculated the homeostatic equilibrium for 8000 randomly placed cells on a $2000 \times 2000 \mu\text{m}$ sheet. As shown in Fig. 5 (blue histogram), this resulted in an equally shaped, skewed distribution of firing rates.

Two other variants of diffusion and cell placement are also shown in Fig. 5: $9 \cdot 10^4$ randomly placed cells in a cube of 1mm^3 , and a single, flat layer of 8000 cells (random x- and y-position, fixed z-coordinate) in a $2000 \times 2000 \times 1000 \mu\text{m}$ cuboid. While the former case mimics a uniform neuronal structure, the latter was meant to mimic interaction solely across a single cortical layer. All other diffusion parameters (λ and D) were kept at their standard values. The resulting firing rate distributions are depicted in Fig. 5. Both variants in 3D space yielded similar distributions, which, however, differed from the original setup with respect to variance and skewness, both being reduced.

Given the good predictions of firing rates of our simplified mathematical model under the standard configuration, these additional predictions suggest the implementation of a full network simulation combined with 3D diffusion for further testing of the homeostatic model. Apparently, the fact that diffusion in three dimensions results in a more localized fundamental solution of a single point source compared to two dimensions leads to a reduced intercellular overlay of homeostatic signals. We also noticed that the width of the distributions could not be further broadened artificially by increasing the diffusion constant to very high values.

Low-density neighborhoods correlate with strong outgoing connections

We previously stated that diffusive homeostasis allowed the network to develop few neurons with exceptionally strong outgoing weights. We found this effect to be present in neurons with an highly above-average firing rate. Moreover, our analytical predictions of individual neuronal activity suggest that the steady state of firing rates is strongly influenced by the spatial structure of excitatory neurons. Combining these two qualities led us to the conclusion that one should be able to observe some relation between spatial structure and the emergence of “driver neurons”. More specific, regions of neurons with above average firing rates should develop stronger outgoing connections. We approximated the local neuron density by means of a Gaussian kernel with $\sigma = 50 \mu\text{m}$ to test this hypothesis. Fig. 6 shows the results. Despite a certain amount of randomness, our prediction was indeed verified.

Discussion

By implementing diffusive homeostasis into the LIF-SORN model, we managed to achieve a broader, skewed firing rate distribution of excitatory cells. In order to acquire a deeper understanding of the mechanisms that determine these statistics we developed an analytical expression that allowed us to reliably predict the steady-state of firing

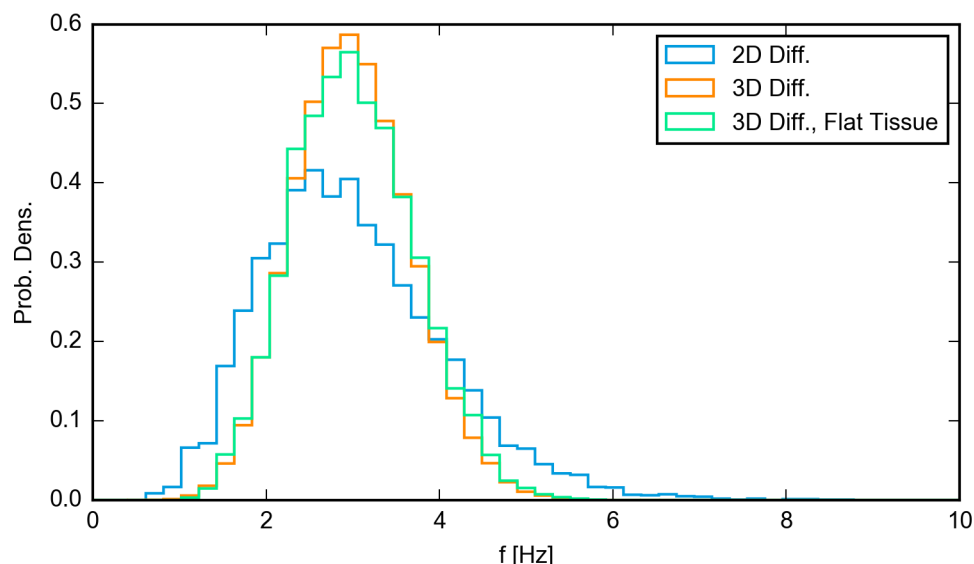


Fig 5. Distribution of firing rates acquired by solving the diffusive homeostatic fixed point. 2D variant was carried out on a $2000 \times 2000 \mu\text{m}$ sheet (grid resolution 200×200) and 8000 randomly picked cell positions. 3D variant used a $1000 \times 1000 \times 1000 \mu\text{m}$ cube (grid resolution $100 \times 100 \times 100$) and $9 \cdot 10^4$ random cell positions. 3D variant with a flat neural tissue used a $2000 \times 2000 \times 1000 \mu\text{m}$ cube (grid resolution $200 \times 200 \times 100$) and 8000 cell positions with random x- and y-coordinates and a z-coordinate fixed at $500 \mu\text{m}$. All graphs depict single-trial data.

rates based on the spatial structure of excitatory neurons. We would like to emphasize that this explanation differs from common approaches of understanding the emergence of heavy-tailed statistics of firing rates in recurrent networks. Theoretical studies on the behavior of recurrent networks are largely based on the assumption that the excitability of neurons is not individually fine-tuned but rather randomly distributed and adjusted globally to achieve a desired mean firing rate. Predictions about the resulting activity are then made based on (potentially simplified) statistical features of recurrent connectivity and/or the specific form of the neuronal transfer function used in the model, see e.g. [41–43]. Our interpretation of our results led us to the conclusion that this approach matches the limiting case of instantaneous diffusion: While Fig. 1A–D did not reveal many differences between finite-velocity and instantaneous diffusion in terms of overall statistics, the decorrelation shown in Fig. 4C suggests that increasing the diffusion constant goes along with a transition between a spatially determined configuration of excitatory firing rates and a network topology-determined behavior.

By analyzing network activity based on our analytic model, we found that indeed only a single homeostatic fixed point exists for finite diffusion constants. On a practical level though, the gradual decorrelation with this theoretical state of activity upon larger values of D was presumably caused by synaptic turnover which changed the synaptic input, since fluctuations of synaptic input were more slowly and less accurately compensated in the case of larger diffusion constants. However, for the standard choice of parameters (being roughly based on experimental data) the resulting activity was indeed strongly bound to the spatial structure of excitatory cells. Naturally, this raised the question of biological plausibility. To our knowledge, no experimental study exists that relates measurements of spontaneous activity to local fluctuations of neuronal densities. Interestingly, measurements in the barrel cortex and hippocampus have found

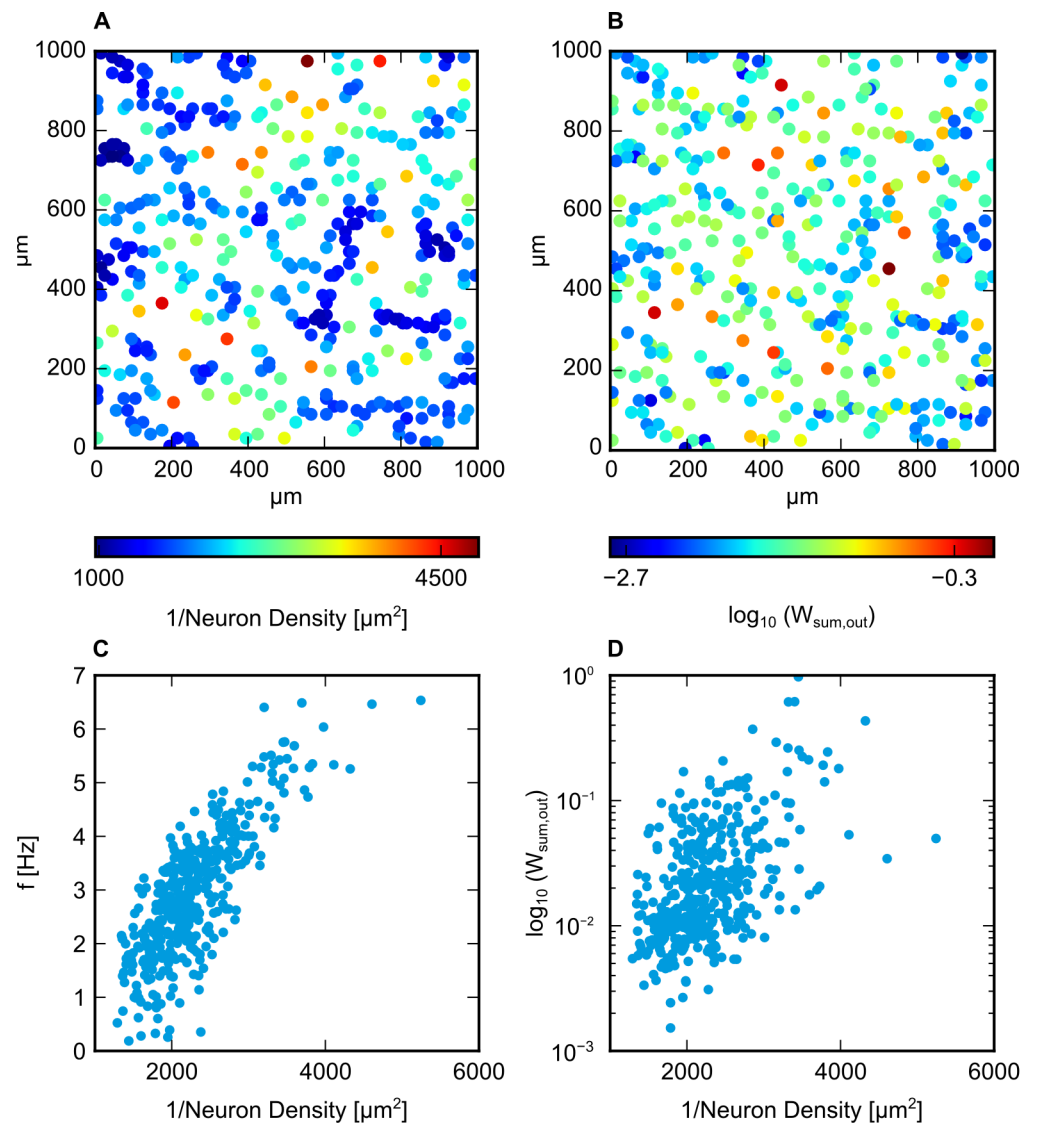


Fig 6. Mean outgoing excitatory weights vs. reciprocal neuron density. **A** and **B**: Scatter-plot of reciprocal local neuron density (calculated by convolution with a Gaussian kernel with $\sigma = 50 \mu\text{m}$) and decadic logarithm of outgoing excitatory weights. Note the spatial correlation in high/low-density regions. **C**: Frequency of excitatory weights (averaged over $1200 \text{ s} \leq t \leq 1500 \text{ s}$) versus reciprocal neuronal density (same estimation method as in A). Coefficient of correlation $\rho_{\text{frequ.}-\text{dens.}} = 0.798$. **D**: Decadic logarithm of mean outgoing excitatory weights versus reciprocal neuronal density. Coefficient of correlation $\rho_{\text{weight.}-\text{dens.}} = 0.513$.

that firing rates during exploration or task performance are significantly correlated with those found for spontaneous, baseline activity [44,45]. This suggests that the same set of neurons tend to be relatively active or inactive under different stimuli and changing environments. In the light of these observations, one might speculate whether random spatial positioning might at least partially act as a determinant of these individual homeostatic working points of firing activity. A possible reason for the strong influence of spatial structure in the implemented model could be the fact that cells were modeled as approximate point sources. This allowed for a clear distinction between individual cells, even in close vicinity. While Sweeney et al. argued that the size of the studied tissue is large compared to the size of individual somata (which, apparently, they claim to be the main source of nitric oxide), Philippides et al. reported that NO is often synthesized in a more delocalized way by means of fine fibers originating from the soma [46]. The diameter of these “production areas” is on the order of 10 – 100μm. This might explain why in reality diffusive homeostasis may not act as much as a precise tuner of single neuron activities as found in the computational model. We have shown that the predictions of our analytic approach to obtaining neuronal firing rates are consistent when using more realistic two-dimensional neuronal densities. Interestingly, the predictions for three-dimensional spatial interaction were less encouraging in terms of broadness and skewness of the resulting firing rate distribution. Still, since some amount of heterogeneity could still be observed, we consider it possible that local bunching or isolation of neurons can induce a disposition towards lower/higher long-term firing rates.

The basic assumption that has to be made for this prediction to hold is that NO concentrations are tuned towards a target concentration across neuronal cell bodies. In the theoretical model we used, this was achieved by tuning neuronal excitability by means of a perfect integral control. This might be considered an oversimplification, but does reflect the general idea that NO concentrations must be held within some regime associated with normal neuronal activity. In consequence, it is reasonable to assume that the aforementioned implications of varying neuronal densities still hold at least qualitatively, even if the tuning of NO concentration is not as strict and exact as seen in the theoretical model.

Savin et al. showed that local lesions in a network subject to diffusive synaptic homeostasis can lead to significantly different, bursting network behavior [47]. This complements our results in the sense that it supports the general idea of diffusive processes affecting activity based on spatial inhomogeneities.

Despite these considerations regarding the effects of spatial structure onto individual firing rates, our modifications seem to be a plausible way of giving rise to many features of cortical structure and activity. Apart from the previously discussed properties of spiking activity, we have shown that important features of synaptic topology and plasticity found in earlier research are compatible with diffusive homeostasis. We thereby created a model, which combines the here presented features of cortical structure with the desired statistics of neuronal activity, based on biologically realistic mechanisms. This was achieved without specific modifications of Hebbian plasticity rules, which have also been proposed as an explanation for log-normally distributed synaptic weights [4,43,48]. Sweeney et al. also included synaptic plasticity via STDP into their model, but did not include synaptic normalization, which led to a bimodal distribution of weights, instead of the log-normal shape we found [20].

In addition, we found that heterogeneity of firing rates led to a much more pronounced separation of mean outgoing weights in our network, which were positively correlated to presynaptic firing rates. This is in line with other theoretical and experimental observations, arguing that a small subset of highly active neurons may serve to form relatively strongly connected and stable subnetworks that can quickly

react to momentary changes in the environment, while fine tuned adaptation involves the slower firing majority of cells [15, 34, 49].

Recent studies have brought up inhibitory-to-excitatory STDP with respect to stabilizing network activity [7, 50]. Results similar to ours concerning network topology have also been achieved with inhibitory STDP [4]. However, we do not regard these similarities as competing explanatory approaches. In terms of their functional role of stabilizing network activity, it is reasonable to assume that both, diffusive homeostasis and inhibitory STDP, can simultaneously act in a biological system.

Conclusion

Our main goal of implementing diffusive homeostasis was to allow a broad distribution of firing rates across the excitatory population of the LIF-SORN, since experimental research has shown this to be an extensively observable phenomenon in the cortex. The implementation of diffusive homeostasis can be regarded as a success with respect to this feature. Furthermore, we did not observe any breakdown of previously studied desirable features of network topology, emerging from the plasticity mechanisms included.

Our theoretical considerations regarding the steady state of firing activity allowed us to further clarify the actual determinants of the resulting firing rate statistics. It turned out that, depending on the choice of diffusion parameters, a weighted mixture between the distribution of neural inputs and the spatial configuration underlies the resulting statistics of firing rates. The former aspect is in line with common theoretical approaches of explaining firing rate distributions. The latter aspect can be subsumed by the hypothesis that local fluctuations of neuronal density can influence firing rates and shape their overall distribution. This was a rather unconventional idea, and we had to leave the question of biological plausibility unanswered and open to experimental research and possibly more detailed theoretical models of nNOS and its influence onto neural activity.

The implementation of diffusive homeostasis led to an interesting observation regarding network structure: Due to the broad range of neuronal activity it allowed for the emergence of highly influential subgroups of excitatory neurons. This feature was not present in earlier versions of the LIF-SORN. It can be regarded as another non-random property of cortical structure that was not hard-coded but naturally emerged from the set of basic rules that constitute dynamics and behavior of our network.

As mentioned previously, the SORN has also proven its capabilities in associative learning and inference tasks [14]. A logical step should thus be to test whether the new features presented in this paper can enhance performance in learning, in the sense that the computational and memory resources given by the network size are used more efficiently.

References

1. Lazar A, Pipa G, Triesch J. SORN: a self-organizing recurrent neural network. *Frontiers in Computational Neuroscience*. 2009;3.
2. Savin C, Joshi P, Triesch J. Independent Component Analysis in Spiking Neurons. *PLOS Computational Biology*. 2010;6(4):1–10. doi:10.1371/journal.pcbi.1000757.
3. Tetzlaff C, Kolodziejewski C, Timme M, Wörgötter F. Analysis of Synaptic Scaling in Combination with Hebbian Plasticity in Several Simple Networks. *Frontiers in Computational Neuroscience*. 2012;.
4. Effenberger F, Jost J. Self-Organization in Balanced State Networks by STDP and Homeostatic Plasticity. *PLOS Computational Biology*. 2015;.
5. Zhang LI, Tao HW, Holt CE, Harris WA, Poo M. A critical window for cooperation and competition among developing retinotectal synapses. *Nature*. 1998;395:37–44.
6. Turrigiano GG. The Self-Tuning Neuron: Synaptic Scaling of Excitatory Synapses. *Cell*. 2008;135.
7. Vogels TP, Sprekeler H, Zenke F, Clopath C, Gerstner W. Inhibitory Plasticity Balances Excitation and Inhibition in Sensory Pathways and Memory Networks. *Science*. 2011;334(6062):1569–1573. doi:10.1126/science.1211095.
8. Abbott L, Nelson SB. Synaptic Plasticity: taming the beast. *Nature Neuroscience*. 2000;.
9. LeMasson G, Marder E, Abbott LF. Activity-dependent regulation of conductances in model neurons. *Science*. 1993;259(5103):1915–1917. doi:10.1126/science.8456317.
10. Miner D, Triesch J. Plasticity-Driven Self-Organization under Topological Constraints Accounts for Non-Random Features of Cortical Synaptic Wiring. *PLoS Computational Biology*. 2016;.
11. Zheng P, Dimitrakakis C, Triesch J. Network Self-Organization Explains the Statistics and Dynamics of Synaptic Connection Strength in Cortex. *PLOS Computational Biology*. 2013;.
12. Markram H. A network of tufted layer 5 pyramidal neurons. *Cerebral Cortex*. 1997;7(6):523–533. doi:10.1093/cercor/7.6.523.
13. Song S, Sjöström PJ, Reigl M, Nelson S, Chklovskii DB. Highly Nonrandom Features of Synaptic Connectivity in Local Cortical Circuits. *PLOS Biology*. 2005;3(3). doi:10.1371/journal.pbio.0030068.
14. Hartmann C, Lazar A, Nessler B, Triesch J. Where's the Noise? Key Features of Spontaneous Activity and Neural Variability Arise through Learning in a Deterministic Network. *PLOS Computational Biology*. 2016;11(12):1–35. doi:10.1371/journal.pcbi.1004640.
15. Buzsáki G, Mizuseki K. The log-dynamic brain: how skewed distributions affect network operations. *Nature Reviews Neuroscience*. 2014;.
16. Wohrer A, Humphries MD, Machens C. Population-wide distributions of neural activity during perceptual decision-making. *Progress in Neurobiology*. 2012;.

17. Buzsáki G, Geisler C, Henze DA, Wang XJ. Interneuron Diversity series: Circuit complexity and axon wiring economy of cortical interneurons. *Trends in Neurosciences*. 2004;27.
18. Marsat G, Maler L. Neural Heterogeneity and Efficient Population Codes for Communication Signals. *Journal of Neurophysiology*. 2010;104(5):2543–2555. doi:10.1152/jn.00256.2010.
19. Tripathy SJ, Padmanabhan K, Gerkin RC, Urban NN. Intermediate intrinsic diversity enhances neural population coding. *Proceedings of the National Academy of Sciences*. 2013;110(20):8248–8253. doi:10.1073/pnas.1221214110.
20. Sweeney Y, Kotaleski JH, Hennig MH. A Diffusive Homeostatic Signal Maintains Neural Heterogeneity and Responsiveness in Cortical Networks. *PLoS Computational Biology*. 2015;.
21. Bi G, Poo M. Synaptic Modifications in Cultured Hippocampal Neurons: Dependence on Spike Timing, Synaptic Strength, and Postsynaptic Cell Type. *The Journal of Neuroscience*. 1998;18(24):10464–10472.
22. Froemke RC, Poo M, Dan Y. Spike-timing-dependent synaptic plasticity depends on dendritic location. *Nature*. 2005;434(7030):221–225.
23. Markram H, Wang Y, Tsodyks M. Differential signaling via the same axon of neocortical pyramidal neurons. *Proceedings of the National Academy of Sciences*. 1998;95(9):5323–5328.
24. Connors BW, Gutnick MJ. Intrinsic firing patterns of diverse neocortical neurons. *Trends in Neurosciences*. 1990;13(3):99 – 104. doi:http://dx.doi.org/10.1016/0166-2236(90)90185-D.
25. Benda J, Herz AVM. A Universal Model for Spike-Frequency Adaption. *Neural Computation*. 2003;15(11):2523–2564.
26. Desai NS, Rutherford LC, Turrigiano GG. Plasticity in the intrinsic Excitability of Cortical Pyramidal Neurons. *Nature Neuroscience*. 1999;2:515–520.
27. Dayan P, Abbott LF. *Theoretical Neuroscience*. MIT Press; 2001.
28. Hill A. The possible effects of the aggregation of the molecules of haemoglobin on its dissociation curves. *The Journal of Physiology*. 1910;40:iv—vii. doi:10.1113/jphysiol.1910.sp001389.
29. Philippides A, Husbands P, O'Shea M. Four-Dimensional Neuronal Signaling by Nitric Oxide: A Computational Analysis. *Journal of Neuroscience*. 2000;20(3):1199–1207.
30. Brette R, Goodman D, Stirnberg M. The Brian spiking neural network simulator (Version 1.0) [Computer Software]; 2016. <http://www.briansimulator.org/>. Available from: <http://www.briansimulator.org/>.
31. Team MD. Matplotlib (Version 1.5.3) [Computer Software]; 2016. <https://matplotlib.org/1.5.3/index.html>. Available from: <http://www.briansimulator.org/>.
32. Hoffmann FZ, Triesch J. Non-random network connectivity comes in pairs. *Network Neuroscience*. 2017;.

33. Alstott J. powerlaw: A Python Package for Analysis of Heavy-Tailed Distributions (Version 1.4.1) [Computer Software]; 2017. <https://pypi.python.org/pypi/powerlaw>. Available from: <http://www.briansimulator.org/>.
34. Yassin L, Benedetti BL, Jouhanneau JS, Wen JA, Poulet JF, Barth AL. An Embedded Subnetwork of Highly Active Neurons in the Neocortex. *Neuron*. 2010;68(6):1043 – 1050. doi:<http://dx.doi.org/10.1016/j.neuron.2010.11.029>.
35. Eckmann JP, Jacobi S, Marom S, Moses E, Zbinden C. Leader neurons in population bursts of 2D living neural networks. *New Journal of Physics*. 2008;10. doi:10.1088/1367-2630/10/1/015011.
36. Sjöström PJ, Turrigiano GG. Rate, Timing, and Cooperativity Jointly Determine Cortical Synaptic Plasticity. *Neuron*. 2001;.
37. Feldman D. The Spike-Timing Dependence of Plasticity. *Neuron*. 2012;.
38. Couto RT. Green's functions for the wave, Helmholtz and Poisson equations in a two-dimensional boundless domain. *Revista Brasileira de Ensino Física*. 2013;.
39. Collins CE, Airey DC, Young NA, Leitch JH D B Kaas. Neuron densities vary across and within cortical areas in primates. *Proceedings of the National Academy of Sciences of the United States of America*. 2010;107.
40. Schüz A, Palm G. Density of neurons and synapses in the cerebral cortex of the mouse. *The Journal of Comparative Neurology*. 1989;286(4):442–455. doi:10.1002/cne.902860404.
41. Roxin A, Brunel N, Hansel D, Mongillo G, van Vreeswijk C. On the Distribution of Firing Rates in Networks of Cortical Neurons. *Journal of Neuroscience*. 2011;31(45):16217–16226. doi:10.1523/JNEUROSCI.1677-11.2011.
42. van Vreeswijk C, Sompolinsky H. Chaotic Balanced State in a Model of Cortical Circuits. *Neural Computation*. 1998;.
43. Koulakov AA, Hromádka T, Zador AM. Correlated Connectivity and the Distribution of Firing Rates in the Neocortex. *The Journal of Neuroscience*. 2009;.
44. O'Connor DH, Peron SP, Huber D, Svoboda K. Neural Activity in Barrel Cortex Underlying Vibrissa-Based Object Localization in Mice. *Neuron*. 2010;67.
45. Mizuseki K, Buzsáki G. Preconfigured, skewed distribution of firing rates in the hippocampus and entorhinal cortex. *Cell Reports*. 2013;4.
46. Philippides A, Ott SR, Husbands P, Lovick TA, O'Shea M. Modeling Cooperative Volume Signaling in a Plexus of Nitric Oxide Synthase-Expressing Neurons. *Journal of Neuroscience*. 2005;25(28):6520–6532. doi:10.1523/JNEUROSCI.1264-05.2005.
47. Savin C, Triesch J, Meyer-Hermann M. Epileptogenesis due to glia-mediated synaptic scaling. *Journal of the Royal Society Interface*. 2008;.
48. Gilson M, Fukai T. Stability versus Neuronal Specialization for STDP: Long-Tail Weight Distributions Solve the Dilemma. *PLOS ONE*. 2011;6(10):1–18. doi:10.1371/journal.pone.0025339.

49. Dragoi G, Harris KD, Buzsáki G. Place Representation within Hippocampal Networks Is Modified by Long-Term Potentiation. *Neuron*. 2003;39(5):843 – 853. doi:[http://dx.doi.org/10.1016/S0896-6273\(03\)00465-3](http://dx.doi.org/10.1016/S0896-6273(03)00465-3).
50. Luz Y, Shamir M. Balancing Feed-Forward Excitation and Inhibition via Hebbian Inhibitory Synaptic Plasticity. *PLOS Computational Biology*. 2012;8(1):1–12. doi:[10.1371/journal.pcbi.1002334](https://doi.org/10.1371/journal.pcbi.1002334).

Supporting information

S1 Appendix. We would like to derive a linear relation between mean firing rate and the mean rate of NO synthesis. One could naively replace the sum of Dirac functions in (9) by a continuous inflow $Ca_{spike}^{2+}r(t)$. This approximation would indeed allow for the correct calculation of a linear relation between mean firing rate and NO production if (10) was a linear homogeneous differential equation. The cubic dependence on Ca^{2+} breaks this simplicity. We note the following in order to derive an approximate description: The target firing rate of 3 Hz and the corresponding mean interspike interval of 0.33...s is large compared to the decay constant of calcium, $\tau_{Ca^{2+}} = 0.01$ s. Consequently, it is very unlikely that one spike event will fall into a region where the calcium concentration, decaying from the instantaneous jump of the previous spike event, is still significantly larger than zero. In fact, calculating the mean concentration of Ca^{2+} before a new spike event over all neurons and all spike events for 1500 s resulted in a value of 0.0013. As such, one can justify the approximation of replacing the exact expression of $Ca^{2+3}(t)$, which is a cubed sum of cut off exponential functions, by a sum of cubed exponentials, because only one term of the sum at a time is significantly larger than zero:

$$Ca^{2+3}(t) = \left[Ca_{spike}^{2+} \sum_i \theta(t - t_{spike}^i) \exp(-(t - t_{spike}^i) / \tau_{Ca^{2+}}) \right]^3 \approx Ca_{spike}^{2+3} \sum_i \theta(t - t_{spike}^i) \exp(-3(t - t_{spike}^i) / \tau_{Ca^{2+}}) \quad (36)$$

with $\theta(x)$ being the Heaviside step function. By the same argument

$$\frac{Ca^{2+3}(t)}{Ca^{2+3}(t) + 1} \approx \sum_i \theta(t - t_{spike}^i) \frac{\exp(-3(t - t_{spike}^i) / \tau_{Ca^{2+}})}{\exp(-3(t - t_{spike}^i) / \tau_{Ca^{2+}}) + \frac{1}{Ca_{spike}^{2+3}}} \quad (37)$$

Therefore, the resulting rate of NO synthesis can be decomposed into a sum of time shifted responses onto a single kernel of calcium concentration as a result of a spike. For a spike at $t_{spike} = 0$, the solution of (10) can be calculated by

$$\begin{aligned} nNOS(t) &= \frac{1}{\tau_{nNOS}} \int_{-\infty}^t dt' \exp(-(t - t') / \tau_{nNOS}) \theta(t') \frac{\exp(-3t' / \tau_{Ca^{2+}})}{\exp(-3t' / \tau_{Ca^{2+}}) + \frac{1}{Ca_{spike}^{2+3}}} \\ &= \frac{1}{\tau_{nNOS}} \int_0^t dt' \exp(-(t - t') / \tau_{nNOS}) \frac{\exp(-3t' / \tau_{Ca^{2+}})}{\exp(-3t' / \tau_{Ca^{2+}}) + \frac{1}{Ca_{spike}^{2+3}}} \end{aligned} \quad (38)$$

The exact solution of this integral can be expressed in terms of the hyper-geometric function, making it rather impractical for any further analysis. Looking for further simplifications, we noted that τ_{nNOS} is ten-fold larger than $\tau_{Ca^{2+}}$. This discrepancy in decay times allows for the assumption that the impact of the calcium kernel onto $nNOS$ is practically instantaneous. Consequently, $nNOS(t)$ becomes

$$nNOS(t) = \frac{1}{\tau_{nNOS}} \theta(t) \exp(-t / \tau_{nNOS}) \int_0^\infty dt' \frac{\exp(-3t' / \tau_{Ca^{2+}})}{\exp(-3t' / \tau_{Ca^{2+}}) + \frac{1}{Ca_{spike}^{2+3}}} \quad (39)$$

In this form, the integral has an easy-to-handle solution, which - with all spike events now included - results in

$$nNOS(t) = \frac{Ca_{spike}^{2+3} \tau_{Ca^{2+}} \ln(2)}{3\tau_{nNOS}} \sum_i \theta(t - t_{spike}^i) \exp(-(t - t_{spike}^i) / \tau_{nNOS}) \quad (40)$$

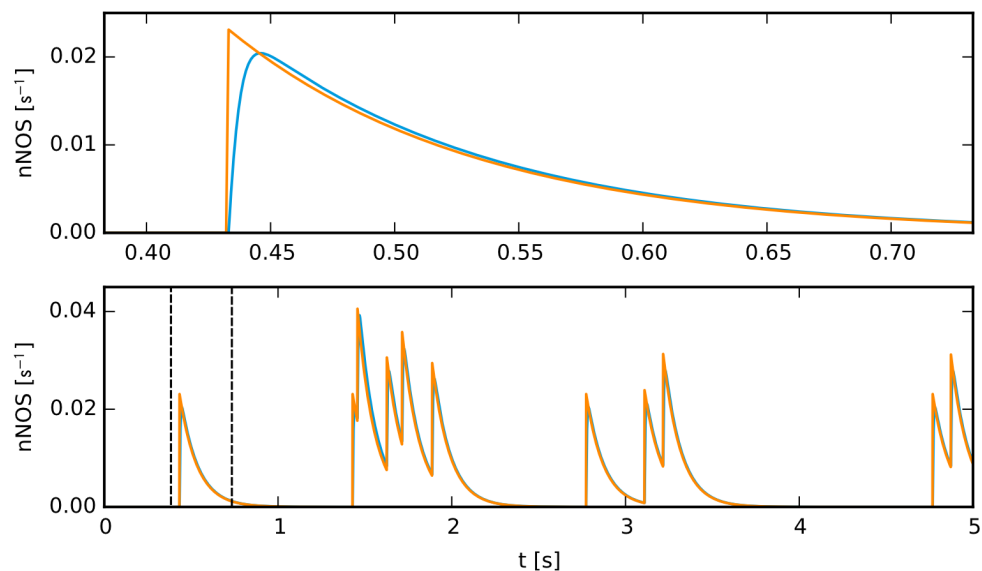


Fig 7. nNOS under Poisson spiking. Time course of $nNOS(t)$ with Poisson spiking at 3 Hz. The full simulation (blue, see equations (9),(10)) is well fitted by the simplified model (red, see Eq. (40)). Top axis is a closeup of the first spike event.

Fig. 7 compares the approximation given by (40) to the full NO production model (equations (9) and (10)). Spikes were drawn from a Poisson process at a rate of 3 Hz. The simplified model fits very well for sufficiently isolated spike events, as predicted. One can observe a slightly smaller but acceptable agreement for the rare event of two subsequent spikes appearing very close to each other, as seen in Fig. 7 at approximately 4 seconds.

Thus, on average, the sum in Eq. (40) simply reduces to the mean rate $\langle r \rangle$:

$$\langle nNOS \rangle = \frac{Ca_{\text{spike}}^{2+} \tau_{Ca^{2+}}^3 \ln(2)}{3\tau_{nNOS}} \langle r \rangle \quad (41)$$